Physics of Fluids ARTICLE pubs.aip.org/aip/pof

On turning maneuverability in self-propelled burst-and-coast swimming

Cite as: Phys. Fluids **36**, 111918 (2024); doi: 10.1063/5.0237171
Submitted: 3 September 2024 · Accepted: 30 October 2024 ·
Published Online: 18 November 2024

Li-Ming Chao,[1,2,3,a)] Iain D. Couzin,[1,2,3] and Liang Li[1,2,3,a)]

AFFILIATIONS

[1]Department of Collective Behaviour, Max Planck Institute of Animal Behavior, Konstanz 78464, Germany
[2]Centre for the Advanced Study of Collective Behaviour, University of Konstanz, Konstanz 78464, Germany
[3]Department of Biology, University of Konstanz, Konstanz 78464, Germany

[a)]**Authors to whom correspondence should be addressed:** chaoliming92@gmail.com and lli@ab.mpg.de

ABSTRACT

Fish have evolved remarkable underwater turning maneuverability, primarily under active control. This allows them to execute turns within confined spaces, such as during C-start rapid turning. In our study, conducted through computational fluid dynamics simulations of a self-propelled swimmer, we revealed that burst-and-coast swimming patterns can generate various turning behaviors purely through passive fluid–body interactions. The burst-and-coast swimming is characterized by the alternating tail movements between continuous undulating burst phases (*bp*) and non-undulating or gliding coast phases (*cp*). Through extensive systematic three-dimensional (3D) simulations, we found that both the burst-and-coast duty cycle—the ratio of burst duration to the total cycle duration—and the swimmer's undulation frequency inhibit turning maneuverability, which is quantified by the curvature of swimming trajectories. We also found there is an optimal Reynolds number that maximizes turning maneuverability. Further analysis suggests that the turning maneuverability is probably due to the persistent presence of the Wagner effect during burst phases and the Magnus effect during coast phases, which differs from the mechanism of actively generating lateral forces by asymmetric continuous flapping. These insights not only advance our understanding of fish locomotion control mechanisms but also provide guidelines for designing underwater robots with improved navigational capabilities.

I. INTRODUCTION

Fish have developed a variety of exceptional abilities in underwater environments throughout evolutionary history.[1–3] One remarkable ability fish have mastered is efficient turning maneuverability, such as during prey capture, predator avoidance, mating, or navigation of complex environments, especially the capability of turning within a limited space.[4]

To achieve turning maneuverability, most fish employ asymmetric kinematics through active flapping control.[5–8] For instance, by asymmetrically controlling their left and right pectoral fins, boxfish (*Ostraciidae*) can turn without horizontal translation, achieving a turning radius close to zero.[9] Rainbow trout (*Salmo gairdneri*) and smallmouth bass (*Micropterus dolomieu*) also demonstrate remarkable turning maneuverability through asymmetrical body and tail movements, achieving minimal turning radii of less than 0.2 body lengths.[10] One extreme example of asymmetric kinematics is the C-start maneuver,[11,12] in which the swimmer rapidly bends its body into a "C" shape and then straightens into a traveling-wavy undulation.

From a hydrodynamic perspective, turning maneuverability that is actively controlled by asymmetric body movements results in unequal forces on both sides, thereby enabling a turn.[13–16] For instance, Schouveiler *et al.* experimentally investigated the generation of horizontal (thrust) and lateral (lift) forces in a tethered flapping foil with both symmetrical and asymmetrical movements.[14] They found that, in the asymmetrical case, a strong lateral force was produced along with a significant decrease in the horizontal force, which is advantageous for maneuvering the propelled vehicle. Studies on the asymmetrical and symmetrical undulation of a simple flapping foil show that asymmetric movement requires more energy compared to the symmetric case.[16] From a control perspective, this turning maneuverability is mostly under active control, where the brain needs to actively send control signals to drive the locomotion muscle, etc.[17]

In this paper, we explore how burst-and-coast swimming, where the oscillation during the burst is completely symmetrical, affects turning maneuverability. Here, burst-and-coast swimming is characterized by the alternating tail movements between continuous undulating

burst phases (*bp*) and non-undulating or gliding coast phases (*cp*).[18,19] Burst-and-coast swimming is a widely observed swimming pattern in fish, including zebrafish (*Danio rerio*),[20] Rummy-nose tetra (*Hemigrammus rhodostomus*),[21] golden shiner (*Notemigonus crysoleucas*),[22] and others. Previous research on burst-and-coast swimming has highlighted its significant energy-saving benefits, demonstrating that it can reduce the cost of transport by over 50% compared to continuous swimming.[23] These findings have been supported by numerous computational studies,[24–31] which have shown potential energy savings of up to 60% and established universal scaling laws for various kinematic parameters influencing energy efficiency in burst-and-coast swimmers.[25]

Here, we used computational fluid dynamics simulations of a self-propelled eel-like (*anguilliform*) swimmer in 3D to investigate how symmetric burst-and-coast kinematics affect turning maneuverability. Our computational model includes four dimensions (X, Y, Z, and yaw) in 3D space. We systematically explored the effects of duty cycle (*DC*), undulation period, and Reynolds number on turning maneuverability, defined as the curvature of the resulting trajectories. In the remainder of the paper, we first described the problem and outlined the employed numerical method in Sec. II. We then presented the main results derived from simulations in Sec. III, with a particular focus on the swimming dynamics generated by the burst-and-coast kinematics. Finally, Sec. IV summarizes the findings of our study and provides a conclusion.

II. PROBLEM DESCRIPTION AND METHODOLOGY

The investigation was performed with a three-dimensional eel-like (*anguilliform*) swimmer.[33] In order to study the fluid dynamic interaction of the flow with the burst-and-coast swimming body, we assumed that the swimmer with a predetermined shape was constructed from elliptical disks with specified axis width and height parameters, following the methodology outlined by Kern and Koumoutsakos.[32] This simplified model reduces the details of the fish muscles and skeleton, such as stiffness, strength limitations, and curvature limitations, and focuses mainly on the hydrodynamic interactions between the body and the surrounding flow. The numerical swimmer was characterized by a body length, denoted as L, and a maximal tailbeat amplitude, A [Fig. 1(b)]. In our study, we maintained a constant dimensionless maximal tailbeat amplitude of $A/L = 0.1$.

During simulations, the swimmer was allowed to swim freely with four degrees of freedom (4-DoF). It had the capability to propel itself in the X, Y, and Z directions with velocities denoted as u, v, and w, respectively, as illustrated in Fig. 1(a). Additionally, the swimmer was capable of yawing with an angular velocity r around its center of mass (COM), while pitching and rolling motions were constrained [Fig. 1(a)]. It should be noted that the conclusions of the present work remain valid when the swimmer is allowed to swim with pitching and rolling motions (6-DoF simulations). More details can be found in Appendix A.

Since fish utilize multiple undulating periods during the *bp*,[29] we defined the swimmer's kinematics as follows:

$$y(x,t) = \begin{cases} f(x,t)\cdot A(x)\cdot \sin\left[2\pi\cdot\left(\dfrac{x}{L}-\dfrac{t}{T_u}\right)\right], & 0 \le t < T_b \\ 0, & T_b \le t < T_b + T_c, \end{cases} \tag{1}$$

where

$$f(x,t) = \begin{cases} 3\cdot\left[\left(\dfrac{t}{T_u}\right)\cdot\left(\dfrac{x}{L}\right)\right]^2 - 2\cdot\left[\left(\dfrac{t}{T_u}\right)\cdot\left(\dfrac{x}{L}\right)\right]^3, & 0 \le t < T_u \\ 1, & T_u \le t < 2T_u \\ 1-3\cdot\left[\left(\dfrac{t}{T_u}\right)\cdot\left(\dfrac{x}{L}\right)\right]^2 + 2\cdot\left[\left(\dfrac{t}{T_u}\right)\cdot\left(\dfrac{x}{L}\right)\right]^3, & 2T_u \le t < T_b \end{cases} \tag{2}$$

is employed to regulate the time-varying envelope of the tailbeat amplitude. The swimmer's kinematics, as described by Eqs. (1) and (2), are inspired by the work of Ashraf *et al.*[34] and Verma *et al.*[35] In the study by Ashraf *et al.*, the authors recorded the undulation of the midline of the tetra fish (*Hemigrammus bleheri*) in a shallow water tunnel and extracted the fish's locomotion as an analytical sinusoidal

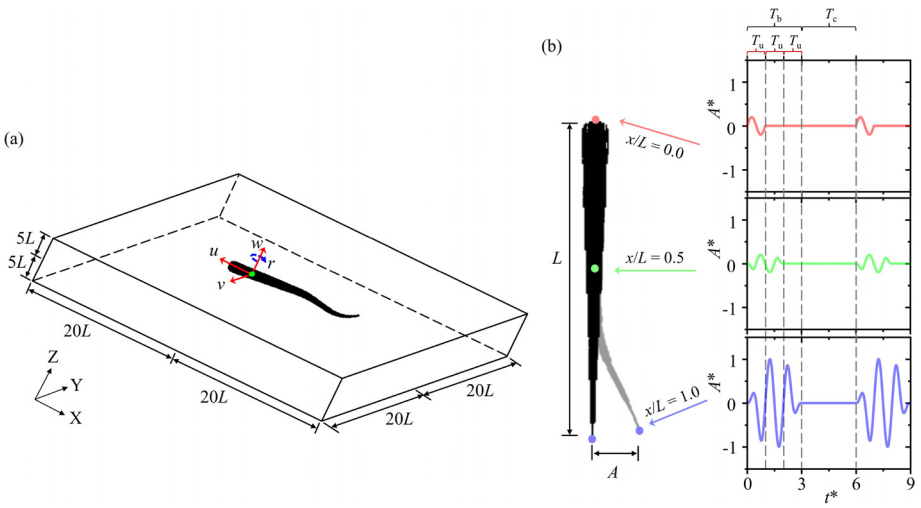

FIG. 1. (a) Sketch of the computational domain, where u, v, and w represent the swimmer's velocity components in the X, Y, and Z directions, respectively, while r denotes the yawing speed. (b) Geometry and kinematics of the swimmer, where the swimmer's geometry follows the parameters used by Kern and Koumoutsakos,[32] L denotes the body length, $A = 0.1L$ stands for the maximal tailbeat amplitude, T_u is the undulation period, T_b corresponds to the duration of the burst phase (*bp*), T_c signifies the duration of the coast phase (*cp*), A^* denotes the normalized undulating amplitude (scaled by A), and t^* represents the normalized time (scaled by T_u), respectively.

traveling wave. In the work of Verma *et al.*, the authors used a piecewise continuous function to control the envelope of the time-varying amplitude of the swimmer, considering four time intervals corresponding to acceleration in the burst phase, steady burst phase, deceleration in the burst phase, and the coast phase.

In our kinematics Eqs. (1) and (2), y represents the instantaneous lateral locomotion, perpendicular to the direction of swimming, while x is measured from the swimmer's head ($0 \le \frac{x}{L} \le 1$). Here, $A(x) = [0.02 - 0.08 \cdot (\frac{x}{L}) + 0.16 \cdot (\frac{x}{L})^2]$ denotes the amplitude function. We also normalized the undulating amplitude $y(x,t)$ using the maximal tailbeat amplitude $A(L)$, denoted as A^*. t represents time. T_b denotes the period of *bp*, and T_c describes the period of the *cp*, with $T_u/T_b = 1/3$ referring to the time period of undulations in one direction and back, respectively. The present definition of kinematics assumes that the swimmer, while undergoing traveling wave kinematics, maintains a constant projected length of the body in the swimming direction. It is important to note that the kinematic equations are defined in the local (body) coordinate system $x - y - z$ of the swimmer, rather than in the global coordinate system X − Y − Z.

Under this definition [Eqs. (1) and (2)], different segments of the swimmer experience varying undulating periods during the *bp*. As depicted in Fig. 1(b), the head of the swimmer undulates over one T_u, while the tail undulates over all T_b ($3T_u$). Unlike previous works,[25,28,30] which typically lead to the synchronized cessation of all swimmer segments, our equations result in a gradual cessation of movement from head to tail, aligning more closely with the characteristics of real fish. Moreover, this definition ensures that the swimmer generates laterally symmetric motion ($\int_0^{T_b} \frac{x}{L} dt = 0$) at arbitrary $\frac{x}{L}$ during the *bp*. Furthermore, we use the duty cycle $DC = T_b/(T_b + T_c)$ to describe the duration of active undulations in burst-and-coast swimming.

The numerical investigations were conducted using the open-source IBAMR software,[36] which is a distributed-memory parallel implementation of the immersed boundary (IB) method.[37–39] This software incorporates the Cartesian grid adaptive mesh refinement (AMR) technique.[40] IBAMR has been extensively applied in the study of fish-like swimming.[31,41–45] In the present simulations, the computational domain was modeled as a rectangular prism measuring $40L \times 40L \times 10L$, with periodic boundary conditions applied along the X, Y, and Z directions [Fig. 1(a)]. Specifically, the Robin boundary conditions implemented using the Structured Adaptive Mesh Refinement Application Infrastructure library have been used to generate the symmetric boundary. In our simulations, the structure is modeled using Lagrangian points, with a total of 29 373 points representing the eel-like swimmer. Furthermore, we used the adaptive mesh refinement (AMR) technique to refine Cartesian grids in the computational domain. Four levels of refinement corresponding to vorticity thresholds of $|\Omega| = 0.5, 1, 2, 4$ were used, and the Cartesian grids would be refined when the magnitude of the fluid vorticity exceeds thresholds. The COM of the swimmer was positioned at the geometric center of the computational domain at $t = 0$. For the grid convergence study, three different grids with uniform mesh spacings of $\Delta X/L = \Delta Y/L = \Delta Z/L = 0.0033$ (M1), 0.001 (M2), and 0.0008 (M3) are considered when $(DC, T_u, Re_u) = (0.5, 1/3\,s, 1500)$. The time step size is fixed at $\Delta t = 10^{-3} T_u$. As shown in Fig. 2, the differences in the time-dependent yawing speed between grids M2 and M3 were negligible. Based on this observation, Grid M2 was selected for the remainder of the simulations, as it provides a balance between accuracy and computational cost. Further convergence studies related to IBAMR have been documented in our previous works[30,46] and publications.[30,41,44] More details about the numerical approach can be found in Bhalla *et al.*[41] The present simulation codes were based on an example from IBAMR, which is available at https://github.com/IBAMR/IBAMR/tree/v0.15.0/examples/ConstraintIB/eel3d. Further codes that support the findings of this study are available upon request from L.-M. Chao.

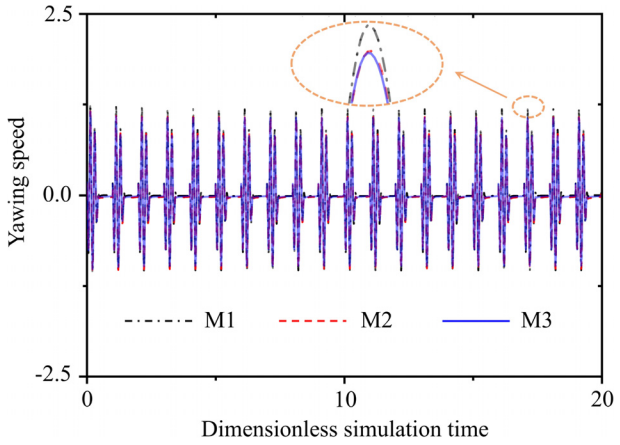

FIG. 2. Grid-convergence study of self-propelled burst-and-coast swimming. M1, $\Delta X/L = \Delta Y/L = \Delta Z/L = 0.0033$; M2, $\Delta X/L = \Delta Y/L = \Delta Z/L = 0.001$; M3, $\Delta X/L = \Delta Y/L = \Delta Z/L = 0.0008$.

III. RESULTS

We conducted examinations of various parameters—duty cycle (DC), undulation period (T_u, in seconds, s), and undulating Reynolds number (Re_u), defined as $Re_u = \frac{AL}{T_u \nu}$, where ν represents the fluid dynamic viscosity—on the hydrodynamic characteristics of the self-propelled swimmer, particularly focusing on turning maneuverability. Here, we varied Re_u by adjusting ν. Drawing insights from studies on the swimming performance of real fish,[2,47,48] we established a baseline condition with parameters $(DC, T_u, Re_u) = (0.5, 1/3s, 1500)$ to assess the impact of varying these parameters. We denoted normalized hydrodynamic quantities obtained in simulations, scaled by their corresponding values under the baseline condition, using the superscript $^+$. Simulations were conducted for a minimum duration of $30(T_b + T_c)$ to ensure statistically steady swimming trajectories, hydrodynamic quantities, and wake structures.

A. Effect of DC, T_u, and Re_u

Figure 3(a) illustrates the swimming trajectories in the X-Y plane of the swimmer propelled by $(T_u, Re_u) = (1/3s, 1500)$ and various DC values ($DC = 0.2, 0.4, 0.5, 0.6, 0.8$, and 1.0), with negligible swimming speed observed in the Z direction ($w \approx 0$). The swimmer clearly exhibits quasi-circle turning paths, particularly noticeable when $DC = 0.2$, in contrast to the straight trajectories observed at continuous gait ($DC = 1.0$) and reported by previous studies on burst-and-coast motion with restricted swimming degrees of freedom (e.g., Refs. 25 and 31 where yawing is typically restricted). This outcome suggests that self-propelled swimmers with 4-DOF can achieve non-straight

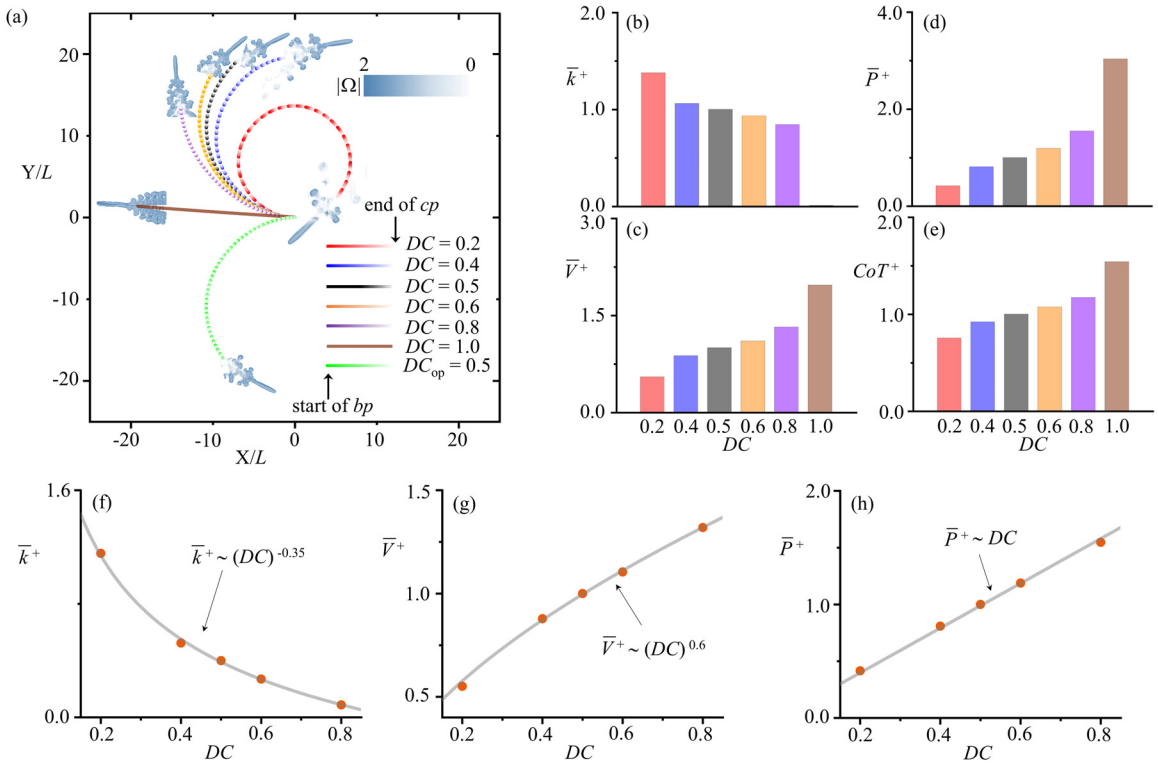

FIG. 3. (a) Swimming trajectories at different DC values when $t = 0 \quad 40(T_b + T_c)$, where $|\Omega|$ denotes the vorticity magnitude, and DC_{op} indicates that the swimmer undulates in the initially opposite direction at $t = 0$. Dependency of normalized averaged (b) curvature $\overline{k}^+$, (c) swimming speed $\overline{V}^+$, (d) power cost $\overline{P}^+$, and (e) cost of transport CoT^+ on DC. Scaling for (f) $\overline{k}^+$, (g) $\overline{V}^+$, and (h) $\overline{P}^+$, respectively. The superscript $^+$ describes normalized hydrodynamic quantities obtained in simulations, scaled by their corresponding values under the baseline condition. $(T_u, Re_u) = (1/3s, 1500)$.

turning using burst-and-coast swimming patterns through fluid–body interaction, and that taking into account yawing is also necessary to generate turning trajectories. Remarkably, a smaller DC, corresponding to longer gliding motions within one burst-and-coast swimming period, induces more pronounced turning motions. Additionally, we noted that the turning direction is influenced by the initial undulating direction. Moreover, we examined the effect of the initial phase ϕ on the swimming trajectory, on the swimming trajectory, focusing on the out-of-phase cases ($\phi = \pi$), denoted by the subscript $_{op}$. In the out-of-phase case, the swimmer's kinematics can be expressed as $y(x,t) = f(x,t) \cdot A(x) \cdot \sin[2\pi \cdot \left(\frac{x}{L} - \frac{t}{T_u}\right) + \pi] \quad \text{for} \quad 0 \le t < T_b$ and $y(x,t) = 0$ for $T_b \le t < T_b + T_c$. As illustrated in Fig. 3(a), the swimming trajectories produced by the $DC = 0.5$ and $DC_{op} = 0.5$ cases are symmetric about the X-axis. This observation suggests that adjusting the initial phase can achieve swimming direction control. Furthermore, the deflection of the swimming trajectories resembles the deflection observed in vortex streets generated by tethered foils.[16,49–52] Using a 2 D heaving foil, Zheng and Wei found that the deflection angle of the vortex street can be correlated with two effective phase velocities, which represent the tendencies of symmetry breaking and symmetry preservation, respectively.[52] Further investigations into the effect of the initial phase on swimming trajectories will be conducted. To assess the turning maneuverability in burst-and-coast swimming, we calculated the averaged curvatures $\overline{k}$ of observed swimming paths from $Y/L = 0$ to $Y/L = 10$, where the bar symbol denotes the time-averaged value. Figure 3(b) illustrates that $\overline{k}^+$ decreases with an increase in DC ($\overline{k}^+ \approx 0$ at $DC = 1.0$), indicating that a smaller DC results in significant turning maneuverability in burst-and-coast swimming, i.e., a smaller turning radius. The linear least squares regression was used to determine the relationship between $\overline{k}^+$ and controlled parameters. Particularly, we found that $\overline{k}^+ \sim DC^{-0.35}$ for our simulation cases [Fig. 3(f)]. These data-based scaling law suggests that $\overline{k} \to \infty$ (zero turning radius) when $DC \to 0$. The condition $DC = 0$ can be related to three scenarios: no undulation, T_u remains constant but T_u goes to infinity, and the swimmer undulating infinitely fast during bp ($T_b \to 0$).[31] The first scenario naturally cannot generate any motion, including turning, while the rest of the scenarios are not realistic in nature.

We further examined the impact of different DC values on the normalized time-averaged speed $\overline{V}^+$ (where $V = \sqrt{u^2 + v^2 + w^2}$), time-averaged power cost $\overline{P}^+$, and the mechanical CoT^+ ($\text{CoT} = \overline{P}/\overline{V}$, see Ref. 53) From the definition of CoT, it is understood that a smaller CoT^+ indicates more efficient swimming. Figures 3(c) and 3(d) demonstrate that a larger DC, corresponding to prolonged burst periods in certain simulation intervals, results in a higher time-averaged speed [Fig. 3(c)] and incurs higher power costs [Fig. 3(d)]. Furthermore, our simulation results indicate that $\overline{V}^+(\overline{V}) \sim DC^{0.6}$

[Fig. 3(g)], which differs slightly from previous research on burst-and-coast pitching foils ($\overline{u} \sim DC^{0.5}$, see Ref. 25). Chao *et al.* found that the pitching motion, considered as the traveling-wavy motion with an extremely large wavelength, can generate higher propulsive force than the undulating traveling-wavy motion,[49] which may explain the difference between our findings and those of Akoz and Moored[25] regarding swimming speed scaling. Both previous research[25] and our findings indicate that $\overline{P}^+(\overline{P}) \sim DC$ [Fig. 3(h)], as the power cost in burst-and-coast swimming is primarily influenced by the effective burst time. As expected, Figs. 3(g) and 3(h) further reveal $\overline{V} \to 0$ and $\overline{P} \to 0$ as $DC \to 0$, respectively. This is because $DC = 0$ resembles no undulation during the *bp*. Figure 3(e) shows that CoT^+ increases with an increase in *DC*, indicating inefficient swimming at larger *DC* values. For the scaling laws related to hydrodynamic performance (swimming speed $\overline{V}^+$ and power cost $\overline{P}^+$), we employed the linear theory to establish the relationship between these quantities and the controlled parameters, as described in our previous work.[46] Additionally, when the swimmer utilizes burst-and-coast kinematics, our definition of kinematics indicates that the tailbeat amplitude is not the same in two consecutive undulation periods, T_b, as shown in Fig. 1(b). However, in continuous kinematics, the swimmer maintains the same tailbeat amplitude over consecutive undulation periods. Therefore, the quantities derived from continuous swimming (i.e., $DC = 1.0$) have not been included in the fitted curves corresponding to burst-and-coast swimming.

The effect of T_u on the swimming behavior was investigated at $DC = 0.5$ and $Re_u = 1500$. Different T_u values result in distinct turning maneuverabilities in burst-and-coast swimming [Fig. 4(a)], with an observed increase in T_u correlating positively with a larger $\overline{k}^+$ calculated within the range of $0 \le Y/L \le 10$ [Fig. 4(b)]. As smaller T_u implies a higher undulation frequency, Fig. 4(b) suggests that a slower undulation enhances turning maneuverability. Moreover, a smaller T_u led to higher power costs [Fig. 4(d)] and faster power transfer into the fluid, resulting in increased swimming speed [Fig. 4(c)]. Using the undulating swimming number $Sw_u = \frac{2\pi LA}{T_u \nu}$ inspired by Ref. 2 scaling laws were derived linking turning maneuverability ($\overline{k}^+$) and hydrodynamic performance ($\overline{V}^+$ and $\overline{P}^+$) to undulating periods, revealing $\overline{k}^+ \sim Sw_u^{0.65}$ [Fig. 4(f)], $\overline{V}^+ \sim Sw_u^{1.33}$ [Fig. 4(g)], and $\overline{P}^+ \sim Sw_u^3$ [Fig. 4(h)], respectively, where hydrodynamic laws are consistent with recent models.[31] According to the definition of Sw_u, $\overline{k}^+$ would approach ∞ as $T_u \to 0$ and approach 0 as $T_u \to \infty$. These two scenarios are analogous to the conditions of $DC = 0$. Furthermore, Fig. 4(e) illustrated that swimming efficiency decreased (CoT^+ increased) as the swimmer undulated with smaller periods T_u.

At $(DC, T_u) = (0.5, 1/3s)$, we examined the influence of fluid dynamic viscosity, represented by the undulating Reynolds number Re_u, on the turning maneuverability and hydrodynamic performance of the self-propelled swimmer by adjusting ν. As Re_u increases, the turning trajectories initially intensify and then diminish [Fig. 5(a)], resulting in an increase followed by a decrease in curvature [Fig. 5(b)],

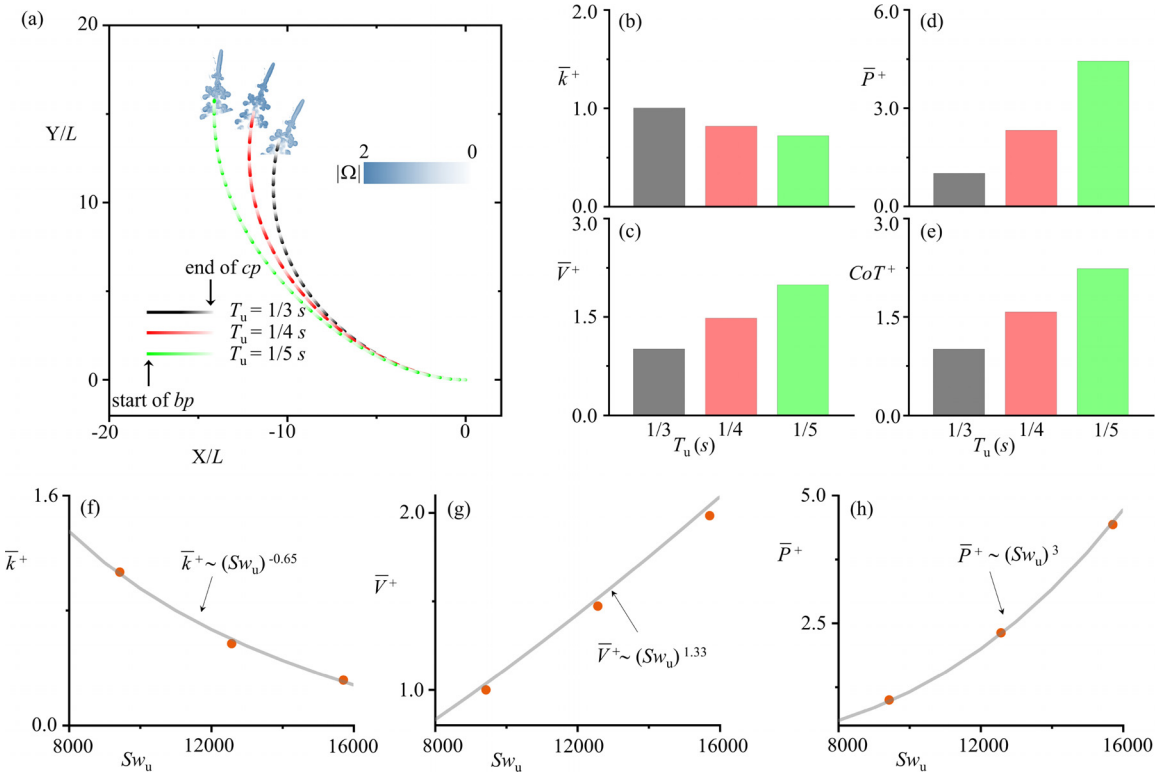

FIG. 4. (a) Swimming trajectories at different T_u s when $t = 0 \quad 30(T_b + T_c)$. Dependence of (b) normalized averaged (b) curvature $\overline{k}^+$, (c) swimming speed $\overline{V}^+$, (d) power cost $\overline{P}^+$, and (e) cost of transport CoT^+ on T_u, respectively. Scaling for (f) $\overline{k}^+$, (g) $\overline{V}^+$, and (h) $\overline{P}^+$, respectively. $Sw_u = 2\pi LA/T_u\nu$. $(DC, Re_u) = (0.5, 1500)$.

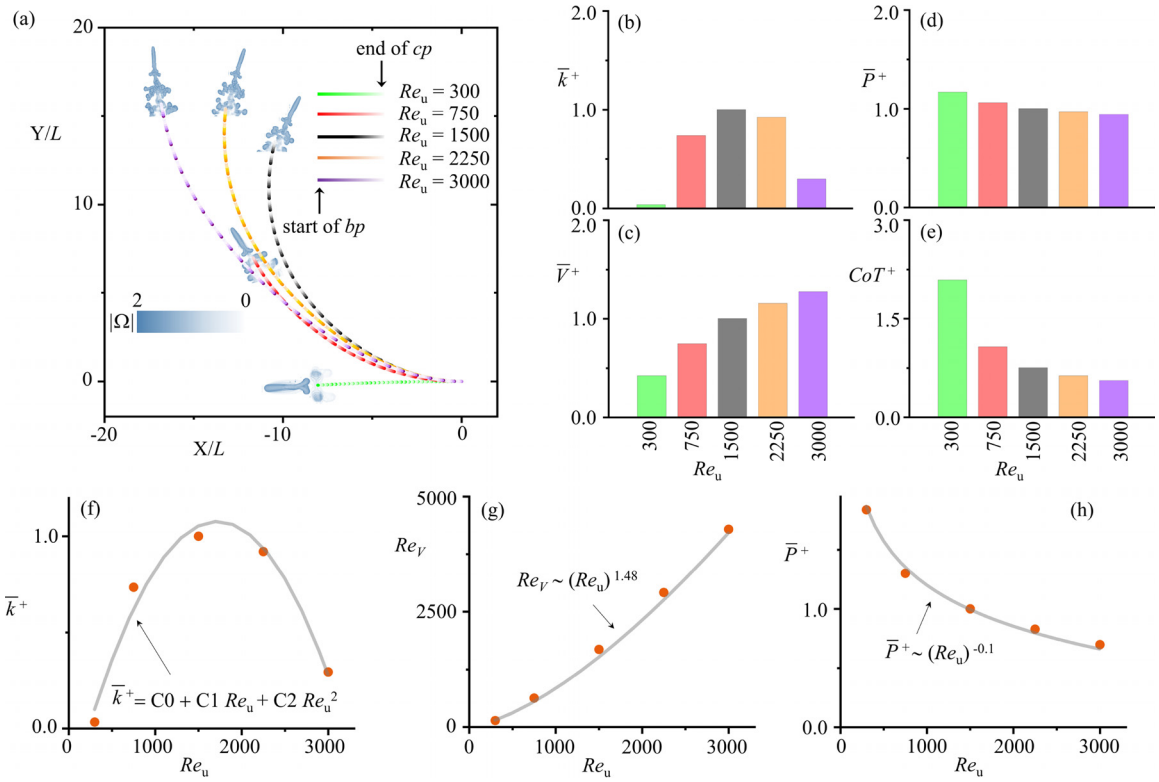

FIG. 5. (a) Swimming trajectories at different Re_u s when $t = 0 \quad 30(T_b + T_c)$. Dependence of normalized averaged (b) curvature $\overline{k}^+$, (c) swimming speed $\overline{V}^+$, (d) power cost $\overline{P}^+$, and (e) cost of transport CoT^+ on Re_u, respectively. Scaling for (f) $\overline{k}^+$, (g) $\overline{V}^+$, and (h) $\overline{P}^+$, respectively. $Re_V = \overline{V}L/\nu$ refers to the swimming Reynolds number. $(DC, T_u) = (0.5, 1/3s)$.

where $\overline{k}^+$ is calculated at $0 \leq Y/L \leq 5$. Notably, when $Re_u = 300$, the swimmer exhibits a quasi-straight trajectory ($\overline{k}^+ \approx 0$), indicating straight-maintaining trajectories under significant viscous effects. Conversely, the swimmer appears to regain its turning motion toward straight motion as Re_u increases (indicating lower fluid dynamic viscosity). As expected, the swimmer attains higher swimming speed with increasing Re_u [Fig. 5(c)], while the power consumption decreases due to reduced viscosity [Fig. 5(d)]. Consequently, swimming efficiency improves, evidenced by a decrease in CoT^+ as Re_u increases [Fig. 5(e)]. Through data fitting, we have shown that there is a polynomial relationship between $\overline{k}^+$ and Re_u [$\overline{k}^+ = C0 + C1Re_u + C2Re_u^2$, where C0, C1, and C2 are fitting constants; Fig. 5(f)], suggesting that an optimal Reynolds number exists for achieving higher turning maneuverability. Moreover, we derived $Re_V \sim Re_u^{1.48}$ [Fig. 5(g)], where $Re_V = \overline{V}L/\nu$ denotes the swimming Reynolds number. This scaling law resembles the relationship between the propulsive Reynolds number and the flapping Reynolds number of continuous flapping foils,[54] indicating that both the continuous and burst-and-coast kinematics share the same scaling law of swimming speed.[55] Moreover, the power cost is fitted as $\overline{P}^+ \sim Re_u^{0.1}$ [Fig. 5(h)].

B. Exploration of turning dynamics

Figure 6(a) illustrates the time history of the normalized yawing speed r^* (scaled by its maximal value) when $(DC, T_u, Re_u) = (0.5, 1/3s, 1500)$, providing insight into the generation of turning maneuverability. The normalized yawing speed, r^*, exhibits an undulating wave pattern resembling the undulating kinematics in the *bp* and forms a decay curve in the *cp*. When the swimmer impulsively starts from rest in the *bp*, the circulation around the swimmer cannot immediately attain a steady-state value, a phenomenon known as the Wagner effect.[56,57] Consequently, the motion in the *bp* yields a non-zero time-averaged yawing speed and provides a non-zero yawing speed at the start of the *cp* [Fig. 6(a)]. During the *cp*, we found that the circulation around the swimmer has a non-zero value, suggesting the presence of the Magnus effect.[58] As a result, the swimmers continuously experience turning trajectories during *cp*. More details about the circulation calculation can be found in Appendix B. Here, the total yawing speeds in the *bp* and *cp* are non-zero, measuring −0.028 and −0.034, respectively. Overall, the Wagner effect generates non-zero time-averaged yawing speed during burst phases, while the Magnus effect maintains turning motion during coast phases. The repeated occurrence of the Wagner effect and Magnus effect during burst-and-coast swimming results in the generation of turning maneuverability [Figs. 3(a), 4(a), and 5(a)]. This occurs without necessitating active kinematic control, such as asymmetric motions of the caudal and pectoral fins.[14,16,59] Conversely, in continuous swimming, the Wagner effect on the yawing speed gradually diminishes, yielding a time-averaged yawing speed of zero,[60] and the Magnus effect can be disregarded. As a result, a swimmer with continuous kinematics is difficult to generate turning maneuverability, as observed in our study.

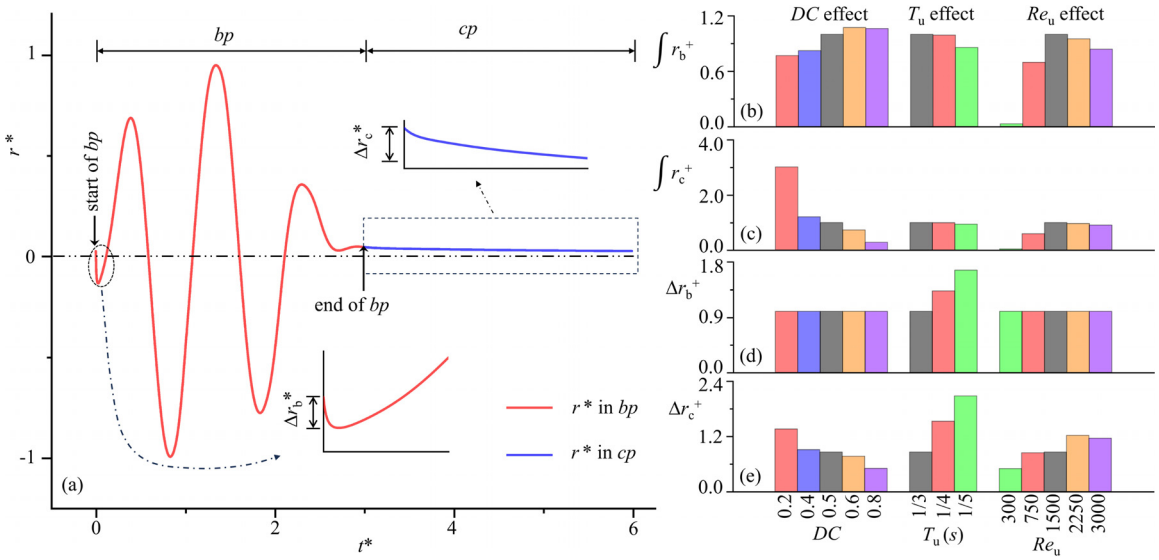

FIG. 6. (a) The time history of the normalized yawing speed r^* (scaled by its maximal value) when $(DC, T_u, Re_u) = (0.5, 1/3s, 1500)$. Δr_b^* describes the r^* jump at the start of the *bp*, Δr_c^* refers to the r^* difference between the end of the *bp* (start of the *cp*) and the end of the *cp*. The *DC*, T_u, and Re_u effect on the total yawing speed $\int r_b^+$ in the *bp* and total yawing speed $\int r_c^+$ in the *cp*, Δr_b^+, and Δr_c^+, are shown in (b) and (e), respectively.

We further investigated the influence of *DC*, T_u, and Re_u on the total yawing speed generated in the *bp* and *cp*, respectively. Figure 6(b) demonstrates that the normalized total yawing speed $\int r_b^+$ generally increases with an increase in *DC* and T_u, with an optimal Re_u corresponding to a larger $\int r_b^+$. Conversely, *DC* significantly affects the normalized total yawing speed $\int r_c^+$ in the *cp*, where a longer coast duration (smaller *DC*) results in a larger $\int r_c^+$ and thus significant turning motion [Fig. 3(a)]. The impulsive start in the *bp* naturally induces a jump in hydrodynamic quantities, such as the yawing speed difference Δr_b^+ shown in Fig. 6(a) and the swimming speed [Fig. 4(b) in Ref. 25] As expected, Δr_b^+ is solely determined by the starting speed ($\sim A/T_u$ at the tail) of the swimmer, where a smaller undulating period results in a larger Δr_b^+ [Fig. 6(d)]. Figure 6(e) illustrates how *DC*, T_u, and Re_u affect the difference in r^* between the end of the *bp* (start of the *cp*) and the end of the *cp*, denoted as Δr_c^+. Δr_c^+ is positively correlated with T_u and Re_u when $Re_u \leq 2250$, but inversely related to *DC*.

C. Wake structures

Figure 7 illustrates the instantaneous wake structures of a self-propelled swimmer with different control parameters *DC*, T_u, and Re_u. Five typical instants are considered: $t^* = 0$ (start of the *bp*), $t^* = 1$, $t^* = 2$, $t^* = 3$ (end of the *bp* or start of the *cp*), and $t^* = 6$ (end of the *cp* or start of a new *bp*). Here, t^* represents the normalized time, scaled by T_u. The three-dimensional vortex structures are visualized by iso-surfaces of the Q-criterion.[61] Generally, the self-propelled swimmer produces a double vortex row located at the left and right sides behind itself. The vortex structures gather at the tail of the swimmer during *bp* ($0 \leq t^* \leq 3$) and shed into the fluid during *cp* ($3 \leq t^* \leq 6$). For burst-and-coast swimming, only double vortex row structures are observed in our work, whereas Borazjani and Sotiropoulos reported that an *anguilliform* swimmer with continuous kinematics could generate both single- and double-row flow patterns.[62] Additionally, the vortex row consists of multiple vortex rings generated during multiple undulation periods T_u, which is different from the single and disconnected vortex rings of the continuous swimmer hypothesized by Müller *et al.*[63]

Figures 7(a) and 7(b) compare the effect of *DC* on vortex generation. The case with $DC = 0.2$ exhibits narrower vortex rings compared to the baseline condition with $DC = 0.5$. This narrower structure results in a concentrated jet flow through the center of the ring, which is advantageous for generating the clockwise turning [Fig. 3(a)]. When T_u decreases, the undulating swimmer introduces more vorticity into the generated vortex. Consequently, a smaller T_u prolongs vortex development and delays vortex pinch-off.[64,65] As a result, the well-organized vortex rings produced in the smaller T_u case [Fig. 7(c)] are much farther apart compared to the baseline condition [Fig. 7(a)], which benefits straight swimming [Fig. 4(a)]. This scenario is also observed at $Re_u = 3000$ [Fig. 7(d)], corresponding to insignificant turning maneuverability [Fig. 5(a)]. These results suggest that an optimal combination of *DC*, T_u, and Re_u is required to produce well-organized vortex rings and powerful jet flow, which strengthen turning maneuverability in burst-and-coast swimming.

IV. CONCLUSIONS

Our study provides a comprehensive analysis of the swimming performance of burst-and-coast organisms, with a particular focus on turning maneuverability. We have demonstrated that burst-and-coast kinematics can induce significant turning trajectories using simulations on a 3D self-propelled swimmer. This finding highlights the role of passive fluid–body interactions, specifically the Wagner effect during burst phases, which generates non-zero yawing speed, and the Magnus effect during coast phases, which exacerbates body rotation, thereby contributing to turning maneuvers. Our investigation into control parameters has revealed that smaller duty cycles and longer

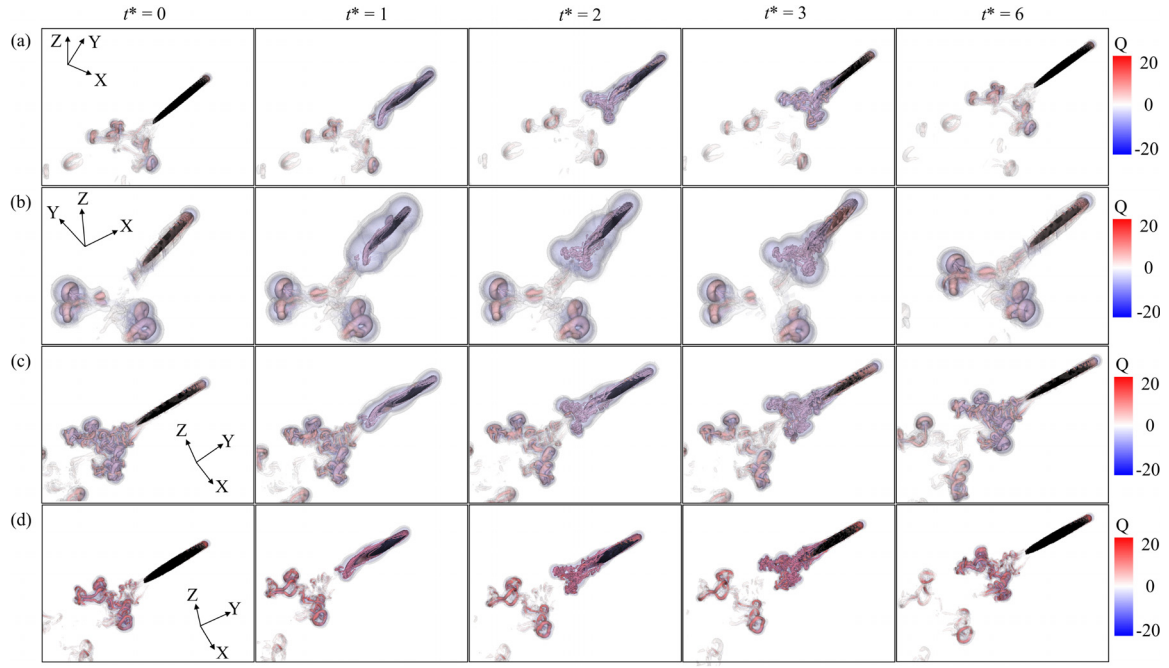

FIG. 7. Three-dimensional vortex structures generated by (a) baseline condition $(DC, T_u, Re_u) = (0.5, 1/3s, 1500)$, (b) $(DC, T_u, Re_u) = (0.2, 1/3s, 1500)$, (c) $(DC, T_u, Re_u) = (0.5, 1/5s, 1500)$, and (d) $(DC, T_u, Re_u) = (0.5, 1/3s, 3000)$, respectively, where five instants, including $t^* = 0$ (start of the *bp*), $t^* = 1$, $t^* = 2$, $t^* = 3$ (end of the *bp* or start of the *cp*), and $t^* = 6$ (end of the *cp* or start of a new *bp*), are illustrated. The flow is visualized by isosurfaces of the Q-criterion.[61]

undulation periods enhance turning maneuverability in burst-and-coast swimming. Furthermore, the effect of the undulating Reynolds number follows a non-straight polynomial trend, indicating an optimal range for maximizing turning maneuverability.

Turning performance is considered a critical aspect of locomotion for many animals.[66] The turning maneuverability achieved by burst-and-coast swimming may offer several advantages for aquatic animals. First, as demonstrated in our study and previous works, burst-and-coast swimming consumes less energy [e.g., Fig. 3(d)], which is beneficial for energy-efficient maneuverability compared with asymmetric kinematics with additional power.[16] Second, while burst-and-coast swimming may result in slower overall swimming speeds [e.g., Fig. 3(c)], it allows fish to gather additional sensory information,[67] such as visual, pressure, and chemical cues, aiding in determining swimming strategies. Finally, by adjusting burst-and-coast kinematics, fish can achieve different turning trajectories, which can be advantageous for both chasing prey and evading predators.

By understanding how swimmers achieve complex locomotion through the interplay of transnational and yawing movements using burst-and-coast kinematics, one can develop robotic systems that mimic these efficient and adaptable swimming strategies. This research not only enhances our knowledge of biological swimming but also informs the engineering of biomimetic robots capable of maneuvering in challenging aquatic environments with improved energy efficiency and agility.

ACKNOWLEDGMENTS

We are grateful to Dr Y. Zou and Dr B. Jin for their insightful discussions on the burst-and-coast behaviors of swimming animals, which greatly enriched our understanding. We acknowledge funding support from the Max Planck Society, the Office of Naval Research N00014-64019-1-2556 (I.D.C.), the European Union's Horizon 2020 research and innovation program under the Marie Skłodowska-Curie Grant Agreement No. 860949 (I.D.C.), the PathFinder European Innovation Council Work Programme 101098722 (I.D.C.), the Struktur-und Innovationsfonds für die Forschung (SI-BW) of the State of Baden-Württemberg, the Deutsche Forschungsgemeinschaft (DFG, German Research Foundation) under Germany's Excellence Strategy-EXC 2117–422037984 (I.D.C.), the Deutsche Forschungsgemeinschaft Gottfried Wilhelm Leibniz Prize 2022 584/22 (I.D.C.), the Sino-German Centre in Beijing for generous funding of the Sino-German Mobility under Grant No. M-0541 (L.L.), and the Messmer Foundation Research Award (L.L.).

AUTHOR DECLARATIONS

Conflict of Interest

The authors have no conflicts to disclose.

Author Contributions

Li-Ming Chao: Conceptualization (equal); Formal analysis (equal); Investigation (equal); Methodology (equal); Software (equal); Validation (equal); Visualization (equal); Writing – original draft (equal); Writing – review & editing (equal). **Iain D. Couzin:** Funding acquisition (equal); Writing – review & editing (equal). **Liang Li:** Formal analysis (equal); Funding acquisition (equal); Writing – review & editing (equal).

DATA AVAILABILITY

The data that support the findings of this study are available from the corresponding author upon reasonable request.

APPENDIX A: COMPARISON BETWEEN 4-DOF AND 6-DOF

Using an example case with $(DC, T_u, Re_u) = (0.5, 1/3\,s, 1500)$, we found that the 4-DoF simulation produced results equivalent to those from the 6-DoF simulation for the purposes of our study. As shown in Fig. 8(a), the trajectories of the swimmer's center of mass (COM) in the X − Y plane from both the 4-DoF and 6-DoF simulations exhibit no significant differences. In the 6-DoF simulation, the pitching and rolling speeds were nearly zero, while the 4-DoF simulation inherently constrained these speeds to zero, as shown in Figs. 8(b) and 8(c). Additionally, both 6-DoF and 4-DoF simulations produced comparable yawing speeds, as shown in Fig. 8(d). Therefore, the conclusions of the present work remain valid when allowing the swimmer to swim with 6-DoF. Given that the 4-DoF simulations require fewer computational resources, we opted for the 4-DoF setup in our simulations.

Moreover, the use of 4-DoF may also be understood from the principle of symmetry. Since the swimmer's kinematics are constrained to the $x - y$ plane and its geometry is symmetric, the swimmer cannot generate pitching and rolling motions. The turning maneuvers observed in the simulations are likely the result of temporal asymmetries during the burst and coast phases, rather than pitching or rolling movements.

APPENDIX B: CALCULATION OF CIRCULATION

Since the swimming speed generated by self-propelled burst-and-coast swimmers in the Z− direction is negligible, we calculate the two-dimensional circulation around the swimmer at a specific slice corresponding to Z = 0. As shown in Fig. 9(a), a square region enclosing the swimmer is selected to calculate the circulation during the coast phase, with the square size set to $2L$. For each line, 100 probes are used to obtain the fluid velocity. The circulation is calculated as

$$\begin{aligned}\Gamma &= \oint_C u_f \cdot \mathrm{dX} + v_f \cdot \mathrm{dY} \\ &= \int_{C_1} v_f \cdot \mathrm{dY} + \int_{C_2} u_f \cdot \mathrm{dX} + \int_{C_3} v_f \cdot \mathrm{dY} + \int_{C_4} u_f \cdot \mathrm{dX}, \end{aligned} \tag{B1}$$

where u_f and v_f refer to the fluid velocity along the path in X− and Y− directions, respectively. The variation of $u_f \cdot \mathrm{dX} + v_f \cdot \mathrm{dY}$ along different paths is shown in Fig. 9(b). As a result, we found $\Gamma = -0.02$, a non-zero value, indicating the presence of the Magnus effect. Additionally, this negative Γ suggests the clockwise turning of the swimmer's trajectory.

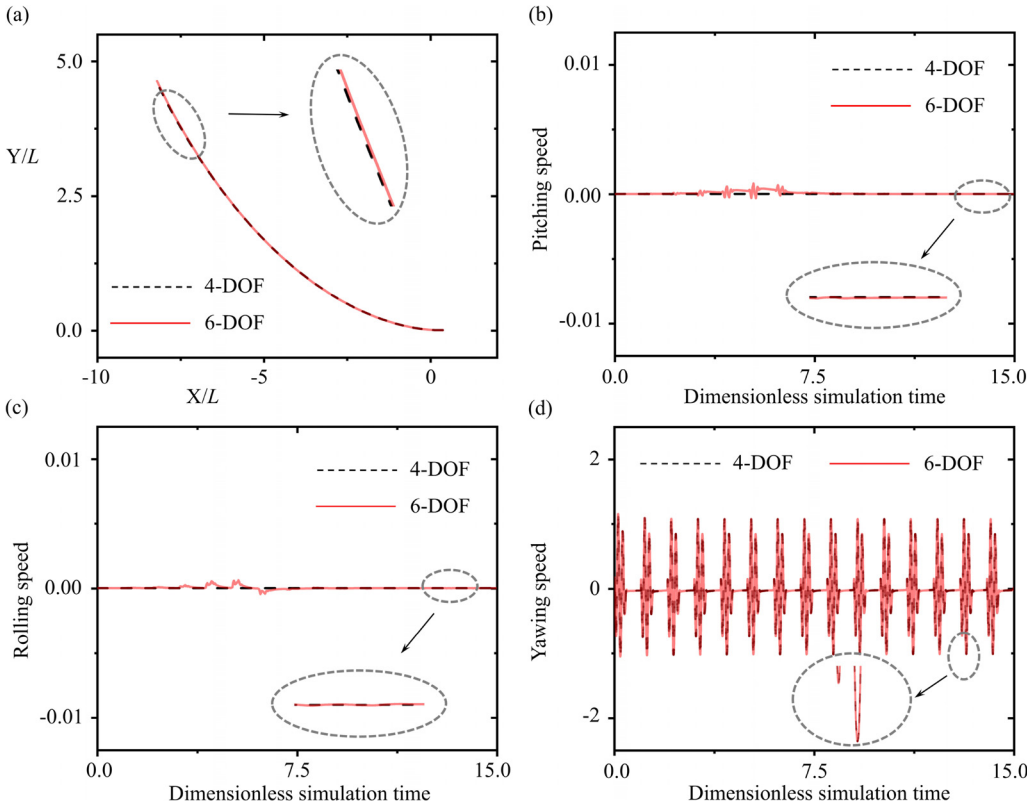

FIG. 8. Comparison of (a) swimming trajectories, (b) pitching speed, (c) rolling speed, and (d) yawing speed when the burst-and-coast swimming is allowed to move with 4-DOF and 6-DOF.

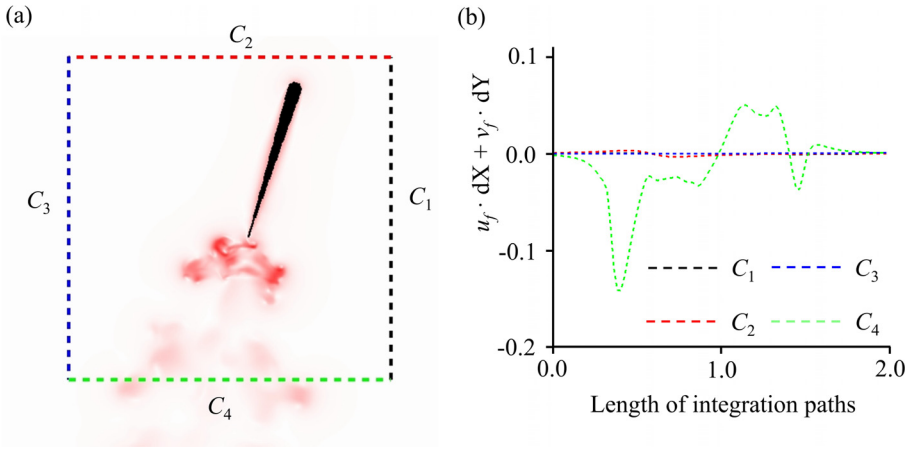

FIG. 9. (a) The paths for line integrals of fluid velocity. (b) The variation of $u_f \cdot dX + v_f \cdot dY$ along the path. Here, u_f and v_f refer to the fluid velocity in X and Y directions, respectively.

REFERENCES

[1]G. K. Taylor, R. L. Nudds, and A. L. R. Thomas, "Flying and swimming animals cruise at a Strouhal number tuned for high power efficiency," Nature **425**, 707–711 (2003).
[2]M. Gazzola, M. Argentina, and L. Mahadevan, "Scaling macroscopic aquatic locomotion," Nat. Phys. **10**, 758–761 (2014).
[3]J. C. Liao, "Fish swimming efficiency," Curr. Biol. **32**, R666–R671 (2022).
[4]U. M. Norberg and J. M. V. Rayner, "Ecological morphology and flight in bats (Mammalia; Chiroptera): Wing adaptations, flight performance, foraging strategy and echolocation," Philos. Trans. R. Soc. London B Biol. Sci. **316**, 335–427 (1987).
[5]P. W. Webb, "Fast-start performance and body form in seven species of teleost fish," J. Exp Biol. **74**, 211–226 (1978).
[6]P. Domenici and R. W. Blake, "The kinematics and performance of fish fast-start swimming," J. Exp Biol. **200**, 1165–1178 (1997).
[7]I. Borazjani, F. Sotiropoulos, E. D. Tytell, and G. V. Lauder, "Hydrodynamics of the bluegill sunfish c-start escape response: Three-dimensional simulations and comparison with experimental data," J. Exp Biol. **215**, 671–684 (2012).
[8]R. Thandiackal and G. V. Lauder, "How zebrafish turn: Analysis of pressure force dynamics and mechanical work," J. Exp. Biol. **223**, jeb223230 (2020).
[9]R. W. Blake, "On ostraciiform locomotion," J. Mar. Biol. Ass. **57**, 1047–1055 (1977).
[10]P. Webb, "Speed, acceleration and manoeuvrability of two teleost fishes," J. Exp Biol. **102**, 115–122 (1983).
[11]M. Gazzola, W. M. Van Rees, and P. Koumoutsakos, "C-start: Optimal start of larval fish," J. Fluid Mech. **698**, 5–18 (2012).
[12]M. S. Triantafyllou, G. D. Weymouth, and J. Miao, "Biomimetic survival hydrodynamics and flow sensing," Annu. Rev. Fluid Mech. **48**, 1–24 (2016).
[13]D. A. Read, F. S. Hover, and M. S. Triantafyllou, "Forces on oscillating foils for propulsion and maneuvering," J. Fluids Struct. **17**, 163–183 (2003).
[14]L. Schouveiler, F. Hover, and M. Triantafyllou, "Performance of flapping foil propulsion," J. Fluids Struct. **20**, 949–959 (2005).
[15]Q. Xiao and W. Liao, "Numerical study of asymmetric effect on a pitching foil," Int. J. Mod. Phys. C **20**, 1663–1680 (2009).
[16]L.-M. Chao, M. M. Alam, and C. Ji, "Drag–thrust transition and wake structures of a pitching foil undergoing asymmetric oscillation," J. Fluids Struct. **103**, 103289 (2021).
[17]O. H. Hawkins, V. M. Ortega-Jiménez, and C. P. Sanford, "Knifefish turning control and hydrodynamics during forward swimming," J. Exp Biol. **225**, jeb243498 (2022).
[18]J. J. Videler and D. Weihs, "Energetic advantages of burst-and-coast swimming of fish at high speeds," J. Exp Biol. **97**, 169–178 (1982).
[19]R. Blake, "Functional design and burst-and-coast swimming in fishes," Can. J. Zool. **61**, 2491–2494 (1983).
[20]G. Amichay, L. Li, M. Nagy, and I. D. Couzin, "Revealing the mechanism and function underlying pairwise temporal coupling in collective motion," Nat. Commun. **15**, 4356 (2024).
[21]D. S. Calovi, A. Litchinko, V. Lecheval, U. Lopez, A. Pérez Escudero, H. Chaté, C. Sire, and G. Theraulaz, "Disentangling and modeling interactions in fish with burst-and-coast swimming reveal distinct alignment and attraction behaviors," PLoS Comput. Biol. **14**, e1005933 (2018).
[22]Y. Katz, K. Tunstrøm, C. C. Ioannou, C. Huepe, and I. D. Couzin, "Inferring the structure and dynamics of interactions in schooling fish," Proc. Natl. Acad. Sci. USA **108**, 18720–18725 (2011).
[23]D. Weihs, "Energetic advantages of burst swimming of fish," J. Exp. Biol. **48**, 215–229 (1974).
[24]M.-H. Chung, "On burst-and-coast swimming performance in fish-like locomotion," Bioinspir. Biomim. **4**, 036001 (2009).
[25]E. Akoz and K. W. Moored, "Unsteady propulsion by an intermittent swimming gait," J. Fluid Mech. **834**, 149–172 (2018).
[26]E. Akoz, P. Han, G. Liu, H. Dong, and K. W. Moored, "Large-amplitude intermittent swimming in viscous and inviscid flows," AIAA J. **57**, 3678–3685 (2019).
[27]I. Ashraf, S. Van Wassenbergh, and S. Verma, "Burst-and-coast swimming is not always energetically beneficial in fish (hemigrammus bleheri)," Bioinspir. Biomim. **16**, 016002 (2021).
[28]S. Gupta, N. Thekkethil, A. Agrawal, K. Hourigan, M. C. Thompson, and A. Sharma, "Body-caudal fin fish-inspired self-propulsion study on burst-and-coast and continuous swimming of a hydrofoil model," Phys. Fluids. **33**, 091905 (2021).
[29]G. Li, I. Ashraf, B. François, D. Kolomenskiy, F. Lechenault, R. Godoy-Diana, and B. Thiria, "Burst-and-coast swimmers optimize gait by adapting unique intrinsic cycle," Commun. Biol. **4**, 40 (2021).
[30]L.-M. Chao, A. P. S. Bhalla, and L. Li, "Vortex interactions of two burst-and-coast swimmers in a side-by-side arrangement," Theor. Comput. Fluid Dyn. **37**, 505–517 (2023).
[31]D. Yang, J. Wu, K. Khedkar, L.-M. Chao, and A. P. S. Bhalla, "Hydrodynamics and scaling laws for intermittent s-start swimming," J. Fluid Mech. **984**, A2 (2024).
[32]S. Kern and P. Koumoutsakos, "Simulations of optimized anguilliform swimming," J. Exp Biol. **209**, 4841–4857 (2006).
[33]P. W. Webb, "Form and function in fish swimming," Sci. Am. **251**, 72–83 (1984).
[34]I. Ashraf, T. Bradshaw, J. Ha, R. Godoy-Diana, and B. Thiria, "Simple phalanx pattern leads to energy saving in cohesive fish schooling," Proc. Natl. Acad. Sci. USA **114**, 9599 (2017).
[35]S. Verma, P. Hadjidoukas, P. Wirth, and P. Koumoutsakos, "Multi-objective optimization of artificial swimmers," in *2017 IEEE Congress on Evolutionary Computation (CEC)* (IEEE, 2017) pp. 1037–1046.
[36]IBMAR, "IBAMR: An adaptive and distributed-memory parallel implementation of the immersed boundary method," https://ibamr.github.io/ (2014).
[37]C. S. Peskin, "The immersed boundary method," Acta. Numer. **11**, 479–517 (2002).
[38]R. Mittal and G. Iaccarino, "Immersed boundary methods," Annu. Rev. Fluid Mech. **37**, 239–261 (2005).

[39]B. E. Griffith and N. A. Patankar, "Immersed methods for fluid–structure interaction," Annu. Rev. Fluid Mech. **52**, 421–448 (2020).
[40]B. S. Kirk, J. W. Peterson, R. H. Stogner, and G. F. Carey, "libMesh: A C++ library for parallel adaptive mesh refinement/coarsening simulations," Eng. Comput. **22**, 237–254 (2006).
[41]A. P. S. Bhalla, R. Bale, B. E. Griffith, and N. A. Patankar, "A unified mathematical framework and an adaptive numerical method for fluid–structure interaction with rigid, deforming, and elastic bodies," J. Comput. Phys. **250**, 446–476 (2013).
[42]E. D. Tytell, M. C. Leftwich, C.-Y. Hsu, B. E. Griffith, A. H. Cohen, A. J. Smits, C. Hamlet, and L. J. Fauci, "Role of body stiffness in undulatory swimming: Insights from robotic and computational models," Phys. Rev. Fluids **1**, 073202 (2016).
[43]D. Zhang, G. Pan, L.-M. Chao, and Y. Zhang, "Effects of Reynolds number and thickness on an undulatory self-propelled foil," Phys. Fluids. **30**, 071902 (2018).
[44]A. P. Hoover, R. Cortez, E. D. Tytell, and L. J. Fauci, "Swimming performance, resonance and shape evolution in heaving flexible panels," J. Fluid Mech. **847**, 386–416 (2018).
[45]N. K. Patel, A. P. S. Bhalla, and N. A. Patankar, "A new constraint-based formulation for hydrodynamically resolved computational neuromechanics of swimming animals," J. Comput. Phys. **375**, 684–716 (2018).
[46]L.-M. Chao, L. Jia, and L. Li, "Tailbeat perturbations improve swimming efficiency in self-propelled flapping foils," J. Fluid Mech. **984**, A46 (2024).
[47]A. C. Gleiss, S. J. Jorgensen, N. Liebsch, J. E. Sala, B. Norman, G. C. Hays, F. Quintana, E. Grundy, C. Campagna, A. W. Trites, B. A. Block, and R. P. Wilson, "Convergent evolution in locomotory patterns of flying and swimming animals," Nat. Commun. **2**, 352 (2011).
[48]J. Sánchez-Rodríguez, C. Raufaste, and M. Argentina, "Scaling the tail beat frequency and swimming speed in underwater undulatory swimming," Nat. Commun. **14**, 5569 (2023).
[49]L.-M. Chao, M. M. Alam, and L. Cheng, "Hydrodynamic performance of slender swimmer: Effect of travelling wavelength," J. Fluid Mech. **947**, A8 (2022).
[50]R. Godoy-Diana, J.-L. Aider, and J. E. Wesfreid, "Transitions in the wake of a flapping foil," Phys. Rev. E **77**, 016308 (2008).
[51]R. Godoy-Diana, C. Marais, J.-L. Aider, and J. E. Wesfreid, "A model for the symmetry breaking of the reverse Bénard–von Kármán vortex street produced by a flapping foil," J. Fluid Mech. **622**, 23–32 (2009).
[52]Z. C. Zheng and Z. Wei, "Study of mechanisms and factors that influence the formation of vortical wake of a heaving airfoil," Phys. Fluids. **24**, 103601 (2012).
[53]R. Bale, M. Hao, A. P. S. Bhalla, and N. A. Patankar, "Energy efficiency and allometry of movement of swimming and flying animals," Proc. Natl. Acad. Sci. USA **111**, 7517–7521 (2014).
[54]X. Lin, J. Wu, and T. Zhang, "Self-directed propulsion of an unconstrained flapping swimmer at low reynolds number: Hydrodynamic behaviour and scaling laws," J. Fluid Mech. **907**, R3 (2021).
[55]A. Das, R. K. Shukla, and R. N. Govardhan, "Universal scaling laws for propulsive performance of thrust producing foils undergoing continuous or intermittent pitching," Fluids **7**, 142 (2022).
[56]P. B. Walker, "Experiments on the growth of circulation about a wing and an apparatus for measuring fluid motion," Report No. 1402 (Aeronautical Research Committee, 1931).
[57]S. P. Sane, "The aerodynamics of insect flight," J. Exp Biol. **206**, 4191–4208 (2003).
[58]J. Seifert, "A review of the magnus effect in aeronautics," Prog. Aerosp. Sci. **55**, 17–45 (2012).
[59]E. G. Drucker and G. V. Lauder, "Function of pectoral fins in rainbow trout: Behavioral repertoire and hydrodynamic forces," J. Exp Biol. **206**, 813–826 (2003).
[60]J. Carling, T. L. Williams, and G. Bowtell, "Self-propelled anguilliform swimming: Simultaneous solution of the two-dimensional Navier–Stokes equations and Newton's laws of motion," J. Exp Biol. **201**, 3143–3166 (1998).
[61]J. C. R. Hunt, A. A. Wray, and P. Moin, "Eddies, streams, and convergence zones in turbulent flows," in Studying Turbulence Using Numerical Simulation Databases, 2. Proceedings of the 1988 Summer Program (1988).
[62]I. Borazjani and F. Sotiropoulos, "Numerical investigation of the hydrodynamics of anguilliform swimming in the transitional and inertial flow regimes," J. Exp Biol. **212**, 576–592 (2009).
[63]U. K. Müller, J. Smit, E. J. Stamhuis, and J. J. Videler, "How the body contributes to the wake in undulatory fish swimming: Flow fields of a swimming EEL (Anguilla Anguilla)," J. Exp Biol. **204**, 2751–2762 (2001).
[64]J. O. Dabiri, "Optimal vortex formation as a unifying principle in biological propulsion," Annu. Rev. Fluid Mech. **41**, 17–33 (2009).
[65]A.-L. Yang, L.-B. Jia, and X.-Z. Yin, "Formation process of the vortex ring generated by an impulsively started circular disc," J. Fluid Mech. **713**, 61–85 (2012).
[66]P. Domenici, "The scaling of locomotor performance in predator–prey encounters: From fish to killer whales," Comp. Biochem. Physiol. A: Mol. Integr. Physiol. **131**, 169–182 (2001).
[67]D. L. Kramer and R. L. McLaughlin, "The behavioral ecology of intermittent locomotion," Am. Zool. **41**, 137–153 (2001).